UC Berkeley

UC Berkeley Previously Published Works

Title

Long-term electrode behavior during treatment of arsenic contaminated groundwater by a pilot-scale iron electrocoagulation system.

Permalink

https://escholarship.org/uc/item/6cs0937d

Authors

Bandaru, Siva RS
Roy, Abhisek
Gadgil, Ashok J
et al.

Publication Date

2020-05-01

DOI

10.1016/j.watres.2020.115668

Peer reviewed

eScholarship.org Powered by the California Digital Library
University of California

This paper appears in Water Research (2020). DOI:10.1016/j.watres.2020.115668

Long-term electrode behavior during treatment of arsenic contaminated groundwater by a pilot-scale iron electrocoagulation system

Siva R. S. Bandaru[1], Abhisek Roy[2], Ashok J. Gadgil[1], Case M. van Genuchten[3,4]*

[1]Department of Civil and Environmental Engineering, University of California, Berkeley, Berkeley, California, USA

[2]Department of Civil Engineering, Jadavpur University, Kolkata, India

[3]Department of Earth Science - Geochemistry, Faculty of Geoscience, Utrecht University, Utrecht, the Netherlands

[4]Department of Geochemistry, Geological Survey of Denmark and Greenland (GEUS), Copenhagen, Denmark

*corresponding author:
cvg@geus.dk

Keywords: anodic dissolution, electrode surface layers, iron electrocoagulation, arsenic removal, sustainable water treatment

This paper appears in Water Research (2020). DOI:10.1016/j.watres.2020.115668

Abstract

Iron electrocoagulation (Fe-EC) is an effective technology to remove arsenic (As) from groundwater used for drinking. A commonly noted limitation of Fe-EC is fouling or passivation of electrode surfaces via rust accumulation over long-term use. In this study, we examined the effect of removing electrode surface layers on the performance of a large-scale (10000 L/d capacity) Fe-EC plant in West Bengal, India. We also characterized the layers formed on the electrodes in active use for over two years at this plant. The electrode surfaces developed three distinct horizontal sections of layers that consisted of different minerals: calcite, Fe(III) precipitates and magnetite near the top, magnetite in the middle, and Fe(III) precipitates and magnetite near the bottom. The interior of all surface layers adjacent to the Fe(0) metal was dominated by magnetite. We determined the impact of surface layer removal by mechanical abrasion on Fe-EC performance by measuring solution composition (As, Fe, P, Si, Mn, Ca, pH, DO) and electrochemical parameters (total cell voltage and electrode interface potentials) during electrolysis. After electrode cleaning, the Fe concentration in the bulk solution increased substantially from 15.2 to 41.5 mg/L. This higher Fe concentration led to increased removal of a number of solutes. For As, the concentration reached below the 10 μg/L WHO MCL more rapidly and with less total Fe consumed (i.e. less electrical energy) after cleaning (128.4 μg/L As removed per kWh) compared to before cleaning (72.9 μg/L As removed per kWh). Similarly, the removal of P and Si improved after cleaning by 0.3 mg/L/kWh and 1.1 mg/L/kWh, respectively. Our results show that mechanically removing the surface layers that accumulate on electrodes over extended periods of Fe-EC operation can restore Fe-EC system efficiency (concentration of solute removed/kWh delivered). Since Fe release into the bulk solution substantially increased upon electrode cleaning, our results also suggest that routine electrode maintenance can ensure robust and reliable Fe-EC performance over year-long timescales.

This paper appears in Water Research (2020). DOI:10.1016/j.watres.2020.115668

1. Introduction

Nearly 200 million people worldwide are exposed to toxic concentrations of naturally occurring arsenic in groundwater used for drinking (Naujokas et al. 2013). Chronic arsenic exposure causes various types of internal cancers, cardiovascular and reproductive problems, and painful skin lesions that can result in gangrene and amputations (Smith et al. 2002; Smith et al. 1992; Steinmaus et al. 2013). The arsenic crisis is severe in South Asia due to the low income of the population, lack of resources and poor infrastructure of arsenic remediation technologies, especially in rural regions (Johnston et al. 2010; Amrose et al. 2015). Iron electrocoagulation (Fe-EC) is gaining attention as a promising technology to remove arsenic from groundwater in resource-poor settings. This technique is attractive because it has many properties that favor implementation and sustainable operation in rural communities, such as its modular design, low cost, flexible operation, low infrastructure requirements, and amenability to automation (Wan et al. 2011; Kumar et al. 2004; Amrose et al. 2014; Holt et al. 2005). In Fe-EC, a small external DC voltage is applied to Fe(0) plates to produce Fe(II) ions at the anode and $H_{2(g)}$ at the cathode (Lakshmanan et al. 2009; Chen 2004; Moreno et al. 2009). The Fe(II) ions generated at the anode migrate to the bulk solution, where dissolved oxygen (DO) can oxidize Fe(II) to form Fe(III) (oxyhydr)oxide precipitates, which have a strong arsenic sorption affinity (Hug and Leupin 2003). While Fe-EC has been well documented in laboratory studies to effectively remove arsenic to below the World Health Organization (WHO) maximum contaminant limit (MCL) of 10 µg/L (WHO 2018), rigorous field-based investigations of Fe-EC treatment remain poorly documented in the peer-reviewed literature, especially for large-scale plants operated over extended periods. Investigations of pilot-scale treatment systems are essential to characterize and address the technical challenges that arise when treatment methods emerge from the laboratory and begin extended operation in the field.

In the few field-based investigations of Fe-EC systems in the literature, it is commonly reported that resistive rust surface layers form on the surfaces of Fe(0) electrodes over extended operating cycles (Amrose et al. 2014, Hernandez et al. 2019, Timmes et al. 2010, van Genuchten et al. 2016). These surface layers have been proposed to reduce the contaminant removal efficiency (herein defined as the concentration of solute removed per electrical energy delivered; µg/L or mg/L per kWh) of Fe-EC systems. Although some studies have characterized the surface layer mineralogy (Timmes et al. 2010; van Genuchten et al. 2016), the role of surface layer growth on the performance of Fe-EC systems is not well understood. In theory, surface layer growth can impact several aspects of EC treatment. First, electrochemically-generated Fe(II) can be trapped in the electrode surface layer, which would decrease the amount of Fe(II) transported to the bulk solution where it forms Fe(III) precipitates that bind solutes, such as arsenic (As), phosphate (P) and silica (Si). Second, if the surface layer consists of poorly-conducting Fe minerals (e.g. goethite, lepidocrocite), the rust build-up would increase the charge transfer resistance, which increases the electrical energy required to pass current and could increase the interface overpotential enough to favor anodic oxidation of H_2O to O_2 instead of Fe(0) to Fe(II) (van Genuchten et al. 2017). Since the formation and growth of surface layers can decrease the contaminant removal efficiency via these processes, surface layer removal is likely an effective method to increase or maintain the performance of Fe-EC system.

Various techniques to mitigate surface layer growth have been proposed in the literature, such as altering the frequency with which the electrode polarity is reversed, manipulating the electrode storage conditions (air dried vs. wet storage) and periodic removal of the surface layers by mechanical abrasion. Of these methods, mechanical removal of the surface layers seems to be one of the most promising strategies. For example, in a recent extended laboratory study, Muller et al. 2019 found that alternating the electrode polarity at both short and long frequencies increased the surface layer mass relative to maintaining a single polarity and varying the

electrode storage conditions during inactive cycles was ineffective at preventing surface layer growth. By contrast, periodic mechanical electrode cleaning (after days to weeks of operation) effectively restored Fe-EC performance in the lab (Muller et al. 2019) and is an attractive field-based approach because it is simple and requires only minimal, low-cost labor without hazardous chemicals (Amrose et al. 2014; Nikolaev et al. 1982). However, few studies describe how the performance of Fe-EC systems changes as a result of thorough electrode cleaning (i.e. with mechanical abrasion to completely remove hard layers of rust build-up) and no studies have investigated Fe-EC field systems with large electrodes (~18000 cm^2 per electrode) that have operated over extended periods. Understanding how mechanical electrode cleaning impacts the performance of fully-operational Fe-EC systems would help practitioners optimize plant maintenance and operation and can be used to improve predictions of the long-term efficiency of Fe-EC systems.

The objective of this work is to characterize the extent to which deep mechanical cleaning of the electrodes restores the performance of a pilot-scale Fe-EC field system in a case where the electrodes had not been cleaned after two years of use (in operation about 8 hours per day, 2-4 days per week). For the purpose of this work, we use the term "deep cleaning" to indicate thorough surface layer removal by mechanical abrasion with a hand-held angle grinder, followed by thorough electrode washing with water. To this end, we performed a set of experiments at an existing Fe-EC plant actively treating arsenic contaminated groundwater for drinking at a rural school near Kolkata, India. To understand the effect of deep cleaning on Fe-EC system performance, we compared an exhaustive series of chemical (As, Fe, P, Si, Mn, pH, DO) and electrochemical parameters (total cell potential, electrode interface potentials) before and after electrode deep cleaning. We also investigated the macroscopic (>1 mm) surface layer properties using a high-resolution digital camera and determined the surface layer mineralogy and composition using X-ray diffraction (XRD), X-ray absorption spectroscopy (XAS) and wet

chemical techniques. Our results reveal significant improvements in the contaminant removal efficiency and operating costs of Fe-EC treatment following electrode deep cleaning. Our field-based Fe-EC investigation provides important complementary perspectives to results derived from laboratory-based Fe-EC studies, both of which are required for a complete understanding of the potential of Fe-EC to sustainably improve safe water access in rural, arsenic-affected, resource-poor communities.

2. Materials and methods

2.1 Description of the Fe-EC system and field site

The Fe-EC pilot plant is situated at Dhapdhapi High School, West Bengal, India and had been in operation for two years prior to the experiments. To meet the local water demand, the plant was operated for 2-4 days per week during the school year and two days per week when school was out of session. The plant consisted of two steel reactor tanks coated with food grade epoxy paint to house the electrode assembly (~1600 L for each tank; 1270 mm × 1210 mm × 1030 mm). Both reactor tanks contained 16 parallel mild steel plates (IS 2062, cold formed, Shri Hari Industries, Mumbai, India) spaced 50 mm apart, each with dimensions of 1000 mm × 900 mm × 3 mm. These mild steel plates (herein referred to as Fe(0) plates or electrodes for simplicity) were used as received. Figure S1 in the Electronic Supplemental Material (ESM) shows the unused electrodes as received. The 16 electrodes in each reactor tank were connected electrically, such that alternating Fe(0) plates served as anode and cathode (8 anodes and 8 cathodes per tank, Fig. 1). The 16 electrodes in reactor tank 1 (RT1) are numbered as E1 to E16, and those in reactor tank 2 (RT2) are numbered as E17 to E32. Both reactor tanks were open to the atmosphere (Fig. 1). Before electrolysis, the tanks were filled with 1000 L of contaminated groundwater from a nearby tube well (depth ~32 m) using a submersible pump at a flow rate of 22 L/min. The chemical composition of this groundwater is summarized in Table S1 in the ESM, but notably contained 164±9 μg/L As.

2.2 Fe(0) electrolysis

We followed the exact Fe-EC electrolysis protocol as employed by the local Fe-EC plant operators. After filling the reactor tanks, anodic Fe(0) dissolution was initiated by applying a direct current of 150 A (current density, i, = 0.3 mA/cm^2) for approximately 90 min to the 32 electrodes housed in both tanks with a custom-built power supply (Suresh Electrical Industries,

India) under ambient atmospheric conditions. A total coulombic dose of 450 C/L (2.3 mM Fe by Faraday's law) was applied in experiments before and after electrode deep cleaning (described below). Following existing practices, we varied the total cell voltage manually to maintain constant current throughout electrolysis. The polarity of all electrodes was reversed after each experiment. During electrolysis, the solution was mixed by recirculating 5.25 reactor volumes per hour using a centrifugal pump. These operating parameters were used in experiments before and after electrode deep cleaning.

2.3 Mechanical removal of the electrode surface layers

Electrode deep cleaning was performed by first removing all Fe(0) plates from the reactor tanks and letting the electrodes air dry overnight on a clean floor cover. When dried, the mass of each electrode plate was measured using a hanging scale (procured locally). Next, selected surface layer sections were sampled for subsequent characterization by gently removing the layers with a brass scraper in the top, middle, and bottom regions of representative Fe(0) plates. Since the solids accumulated on the electrode surface contained several layers, a series of scrapings from the outer and inner layers at a single location was also collected. In addition to surface layer samples, the As-laden Fe(III) precipitate sludge produced during routine Fe-EC treatment was collected from the Fe-EC plant tube settler. The surface layers and raw sludge were stored in clean-sealed plastic bags prior to analysis by X-ray diffraction (XRD), X-ray absorption spectroscopy (XAS) and acid digestions.

After collecting surface layer samples from >10 different electrodes across both reactor tanks, the remaining surface layers were removed from each electrode using angle grinders fit with a metallic wire brush for removing rust from steel. To maintain the structural integrity of the electrodes during deep cleaning, minimal pressure was applied while using the angle grinders. After electrode deep cleaning, each Fe(0) plate was rinsed with water to remove

residual surface flakes and the electrodes were left to dry overnight. The mass of each electrode was then measured again using a hanging scale to quantify mass loss from deep cleaning. A high-resolution digital camera was used to photograph the electrodes before and after deep cleaning. The electrodes were then re-inserted into their respective positions in the reactor tanks and were reconnected to the power supply.

2.4 Solid phase analysis

Major and minor mineral phases in the surface layers were identified by powder XRD and XAS. For XRD, the surface layer samples were ground into a fine powder with a mortar and pestle. A Bruker D-8 diffractometer was used to collect the diffractograms (Cu K-α radiation) from 15-75° 2θ (0.01° step sizes) using a rotating sample stage. X-ray absorption spectra at the Fe K-edge were collected for a subset of samples at beam line 4-1 of the Stanford Synchrotron Radiation Lightsource and at the Dutch-Belgian beam line (DUBBLE, BM-26a) of the European Synchrotron Facility (Nikitenko et al. 2008; Borsboom et al. 1998). Additional details of XAS data collection and analysis are provided in the SI.

The chemical composition of the solids was determined by digesting surface layer samples and the raw treatment sludge using an aqua regia solution (70% HNO_3 and 37% HCl, 1:3 mol ratio) following published protocols (van Genuchten et al. 2016). The digestion was then analyzed for Fe, As, P, Si, Ca, and Mn by inductively-coupled plasma optical emission spectrometry (ICP-OES, Perkin Elmer Optima 8000).

2.5 Bulk solution and electrochemical measurements

A series of water samples was collected at regular time intervals during Fe(0) electrolysis before and after deep cleaning to evaluate the effect of surface layer removal on solution chemistry. While the reactors were filling with groundwater, aliquots of raw, unfiltered water

were collected in 15 mL sample vials for measurements of the initial electrolyte composition. After the current was applied, unfiltered aliquots of the bulk solution were collected using a wide mouth pipette every 10 min during electrolysis for measurements of total Fe generated by Fe-EC. In addition, filtered samples were collected at identical 10 min intervals by passing a suspension aliquot through 0.2 μm nylon filters for measurements of dissolved ions. A few drops of concentrated nitric acid (70%) were added to 5 ml of each filtered and unfiltered sample and the final volume was adjusted to 10 mL by adding DI water. All samples were sealed to the atmosphere and transported to the home institution for analysis of Fe, As, P, Si, Ca, and Mn by ICP-OES.

Bulk solution pH and DO were measured initially and throughout electrolysis using a Thermo Scientific Orion pH meter and Hach LDO optical DO probe, respectively. The initial pH and DO were measured in RT1 at a depth of ~25 cm before initiating electrolysis. During electrolysis, pH and DO measurements were collected at 10 min intervals at the same location in RT1.

The interfacial potentials (IP) of the electrodes (anodes and cathodes) were measured after the current stabilized (10 min after onset of electrolysis) using an Ag/AgCl reference electrode and a handheld multimeter (Fluke). The IP of each electrode was measured by submerging the Ag/AgCl reference electrode to a depth of 12-13 cm and placing the tip of the reference electrode adjacent to the Fe(0) plate. Current flowing through each Fe(0) plate was measured with a handheld AC/DC clamp meter (Fluke 376 True RMS). All measurements except pH and DO are plotted as an average of values from RT1 and RT2. Identical protocols for bulk solution and electrochemical measurements were followed in experiments before and after electrode deep cleaning.

3. Results

3.1 Macroscopic characteristics of the electrodes

Fig. 2 shows the macroscopic surface characteristics of a representative Fe(0) plate before (Fig. 2A) and after (Fig. 2B) electrode deep cleaning. The surface of the Fe(0) plate before cleaning (Fig. 2A) had three visually distinct regions, labeled A-I, A-II and A-III based on color and surface texture. The top (A-I) approximately 1/3 of the plate was characterized by light orange surface layers with smooth uniform texture. The middle (A-II) region, which was also approximately 1/3 of the electrode, showed black surface layers with a heterogeneous texture consisting of large (2-5 cm diameter) oblate, dome-shaped blisters. The bottom (A-III) 1/3 of the electrode was a closer match to the A-I region, but had thicker and dark orange surface layers covered with smaller (<1 cm diameter) blisters. These three distinct regions were observed for both sides of every electrode, except for those at the ends of each electrode assembly (end-plates E1 and E16 in RT1 and E17 and E32 in RT2). The sides of the four end-plates that faced the bulk electrolyte displayed surface layers of uniform light orange color without blisters (Fig. S2). The sides of these end-plates that faced the electrode assembly resembled the remaining electrodes with A-I, A-II and A-III regions.

Electrode deep cleaning (described in Section 2.3) removed significant quantities of the surface layers that had accumulated on the electrodes over two years. On average, 2.3±0.4 kg (Table S2) of surface layers was removed from each electrode, which was >10% of the initial average electrode mass (21.7±0.6 kg). Removing the surface layers resulted in smooth black surfaces for all regions (B-I, B-II and B-III, Fig. 2B). Visual inspection of the electrodes after deep cleaning revealed a near complete transformation of the middle region (B-II) to a black heterogeneous texture, rather than the smooth shiny surface indicative of Fe(0) metal in the B-I and B-III regions. Electrode deep cleaning around large blisters (2-5 cm diameter) resulted in significant material loss in the form of large flakes (1-2 cm diameter, 0.2-0.5 mm thickness),

256 which produced depressions in the electrodes. Additional cleaning around blisters in the middle
257 of the electrode might have resulted in cleaner surfaces (Fig. 2B), but more rigorous cleaning
258 was not attempted in this region to avoid structural damage to the electrode.
259
260 3.2 Surface layer characterization
261 *3.2.1 Mineralogy.* In Fig. 3, we present XRD patterns of surface layer samples from the
262 three characteristic locations (A-I, A-II and A-III) showing different colors and textures for a
263 representative electrode (E31). In addition, Fig. 3 presents the XRD patterns of samples
264 collected at different depths of the surface layer at a single location (E22 exterior, interior). The
265 XRD patterns showed differences in the intensity of characteristic diffraction peaks depending
266 on the sample location and depth. For example, the Bragg diffraction peak of calcite ($CaCO_3$) is
267 more intense in the sample collected from the A-I region of the electrode, which also had the
268 lightest color. Bragg diffraction peaks from goethite (α-FeOOH) and lepidocrocite (γ-FeOOH)
269 were also more apparent in the A-I and A-III surface layers than in the A-II region. Peaks from
270 calcite and lepidocrocite were absent in the XRD pattern of the sample collected from the black
271 middle region (A-II); only peaks due to magnetite (Fe_3O_4) appeared in this diffractogram. The
272 extended X-ray absorption fine structure (EXAFS) spectra of the samples collected from the A-I,
273 A-II and A-III regions showed trends consistent with the XRD patterns, but suggest a larger
274 contribution of disordered Fe(III) precipitates. The EXAFS spectra of the A-I and A-III surface
275 layers display characteristic fingerprints of nanocrystalline 2-line ferrihydrite (Fig. S4), which
276 was not apparent in the diffractograms. The EXAFS spectrum of the A-II surface layer matched
277 more closely that of magnetite. Comparing the diffractograms of samples collected from the
278 interior and exterior of a single location (Fig. 3) showed that the light-colored exterior contained
279 more Fe(III) precipitates and calcite, whereas magnetite dominated the interior adjacent to the
280 Fe(0) metal.

Figure 4 shows the powder XRD patterns of homogenized flakes (~1-3 cm diameter) of surface layers collected from 10 different electrodes. All surface layer samples exhibited diffractograms with similar features, but slightly varied peak amplitudes. The diffractograms indicate that magnetite is a major component of the surface layers, regardless of the plate position in the electrode assembly, but we note that disordered Fe(III) precipitates could be present and not display strong peaks in the XRD patterns. In addition to the widespread presence of magnetite, nearly all surface layer samples showed Bragg peaks from goethite, and to a lesser extent, lepidocrocite, which is consistent with previous studies of the surface layers formed on Fe-EC electrodes over shorter timescales (Timmes et al. 2010; van Genuchten et al. 2016). Bragg diffraction peaks for calcite were observed in many samples, but were more intense in the light-colored samples, consistent with the XRD patterns of A-I surface layers of E31 (Fig. 3).

3.2.2 Chemical composition. In Table 1, we present the chemical composition of identical surface layer samples as those for which XRD patterns are given in Fig. 3. For comparison, Table 1 also lists the chemical composition of the air-dried Fe(III) precipitate bulk sludge collected from the tube settler after one Fe-EC run. Along the height of the plate, the mass fraction of Fe (532 g/kg) was highest in the A-II region, consistent with the predominance of magnetite, which has a higher theoretical Fe mass fraction (724 g/kg for Fe_3O_4) than goethite (629 g/kg for FeOOH) and ferrihydrite (523 g/kg for $Fe(OH)_3$). In contrast, the mass fractions of As (55 mg/kg), Si (3.1 g/kg) and Ca (1.9 g/kg) were lowest in the A-II region. In general, the A-I and A-III regions contained the highest fraction of oxyanions (As = 72-158 mg/kg; Si = 5.4-5.5 g/kg; P = 497-654 mg/kg) and Ca (24.6-42.9 g/kg), which is consistent with the higher fraction of poorly-ordered, reactive Fe(III) precipitates and calcite in these regions. However, Mn had a relatively uniform distribution in the three regions (770-1060 mg/kg). Within a single surface layer, the mass fractions of all elements except Fe were 2-5 times higher at the exterior than the interior (Table 1).

All surface layer samples displayed higher mass fractions of Fe (435-532 g/kg) than the air-dried bulk treatment sludge generated during Fe-EC (186 g/kg Fe). The bulk treatment sludge also contained 3-30 times higher oxyanion mass fractions (Table 1) than any of the surface layers. By contrast, the Ca and Mn mass fractions of the treatment sludge (Ca = 71.3 g/kg; Mn = 885 mg/kg) were relatively similar to the electrode surface layers. The overall trends in surface layer composition tabulated for electrode 31 (E31) in Table 1 were comparable for all measured surface layers collected from other electrodes (Table S2).

3.3 Behavior of the chemical composition of the bulk electrolyte

3.3.1 Iron production. In Fig. 5, we report the average concentration of total Fe (aqueous plus solid phase) measured in the bulk electrolyte throughout electrolysis before and after electrode deep cleaning. The gray bar in Fig. 5 represents the expected bulk Fe concentration based on Faraday's law, assuming all charge passed through the anode goes to the production and release of Fe(II) to the bulk solution (i.e. 100% Faradaic efficiency). Before electrode deep cleaning, the bulk Fe concentration remained near its initial value of 13.7±2.2 mg/L throughout the delivery of 450 C/L, indicating poor production of Fe in bulk solution. By contrast, the bulk Fe concentration after electrode deep cleaning increased roughly linearly with electrolysis time, leading to 41.5 mg/L at the end of electrolysis. Although the Fe level increased substantially after electrode deep cleaning, the 41.5 mg/L measured after cleaning is still below the expected concentration (117.0 mg/L) assuming 100% Faradaic efficiency, which could be due to inadequate mixing during electrolysis and settling of Fe(III) solids. We also note that laboratory experiments using brand new electrodes of the same material as those of the Fe-EC pilot plant in the current investigation measured a Faradaic efficiency in synthetic groundwater of approximately 80% (Muller et al. 2019).

330 *3.3.2 Dissolved arsenic, phosphate, silicate and manganese*. Fig. 6 compares the residual
331 fractions of dissolved As, P, Si and Mn in the bulk solution before and after deep cleaning of
332 electrode. Electrode cleaning resulted in more rapid removal of As, P, Si and Mn. For example,
333 the As concentration decreased from the initial 164±9 µg/L to <10 µg/L within 60 min of
334 electrolysis after electrode deep cleaning, whereas ~90 minutes of electrolysis was required to
335 reach 10 µg/L using uncleaned electrodes. Similar to As removal, the removal of P was
336 improved after electrode deep cleaning. Fig. 6B shows that after 20 min of Fe(0) electrolysis,
337 98% of the initial 1.6±0.3 mg/L P was removed after deep cleaning compared to just 74% at the
338 same stage of electrolysis using uncleaned electrodes. Electrode deep cleaning also resulted in
339 an increase in Si removal (initial Si = 15.3±1.7 mg/L) from nearly no removal with the uncleaned
340 electrodes to 28% removal at the end of electrolysis (Fig. 6C). Consistent with the removal of
341 oxyanions, the removal fraction of initial Mn (5.8±0.3 mg/L) increased from 12% before
342 electrode deep cleaning to 21% (Fig. 6D). Taken together, electrode deep cleaning improved the
343 removal of all measured species per kWh (Table S3).
344
345 3.4 Electrochemical parameters.
346 The behavior of the cell potential as a function of electrolysis time (Fig. 7) was similar
347 for experiments before and after deep cleaning, with a rapid increase in voltage immediately
348 after the onset of electrolysis, followed by a gradual increase. However, the curve of the total
349 cell potential was positioned ~2 V lower for the experiment following electrode deep cleaning
350 (6.2 to 9.9 V) relative to that before cleaning (7.8 to 11.8 V). This lower voltage required to pass
351 the 150 A current resulted in lower energy consumed over the course of electrolysis from 2.2
352 kWh before cleaning to 1.6 kWh after cleaning. Consistent with the reduction in total cell
353 potential after deep cleaning, the average anodic interface potential became less positive,
354 decreasing from 3.0±0.9 to 2.1±0.6 V vs Ag/AgCl for all anodes in RT1 and RT2 (Fig. S5). The

355 average cathodic interface potential also became less negative after deep cleaning (-2.2±0.5 to -
356 1.5±0.5 V vs Ag/AgCl for all cathodes electrodes in RT1 and RT2). Measurements of the
357 current for individual plates (Table S4) indicated the 150 A applied to both RT1 and RT2 was
358 well distributed among all plates (9.7 A per plate) except for those facing the bulk electrolyte
359 (E1, E16, E17, E32), which had less current (7.1 per plate).
360
361 3.5 Dissolved oxygen and pH.
362 Fig. 8 shows the behavior of the DO and solution pH in the bulk electrolyte throughout
363 electrolysis before and after electrode deep cleaning. Consistent with the reducing conditions of
364 the aquifer that provided the raw water, low initial DO concentrations were measured before
365 Fe(0) electrolysis. Before deep cleaning, the DO concentration reached air-saturation (>9 mg/L)
366 after 80 min of electrolysis, where it stayed for the remainder of the experiment. After deep
367 cleaning, the DO level increased more slowly and stabilized near 7 mg/L, several mg/L below
368 the air-saturated value.
369 The behavior of solution pH throughout electrolysis (Fig. 8B) followed similar trends for
370 experiments before and after electrode deep cleaning. In both sets of experiments, the solution
371 pH steadily increased during electrolysis, consistent with cathodic H^+ reduction to $H_{2(g)}$, after a
372 short 15 min lag where it stayed near its initial value of 7.1. Although the shape of the pH curve
373 as a function of electrolysis time was similar for experiments before and after deep cleaning, the
374 increase in pH with electrolysis time was smaller after electrode deep cleaning (final pH near
375 7.5) than before deep cleaning (final pH near 7.7).

4. Discussion

4.1. Physical characteristics of surface layers formed during extended Fe-EC field treatment

4.1.1 Formation of three distinct electrode surface regions. The XRD and XAS data of surface layer samples suggest widespread magnetite formation adjacent to the Fe(0) metal (i.e. the interior surface layer) extending over the entire electrode surface, with layers of calcite and Fe(III) precipitates adhered to the surface layer exterior of the A-I and A-III regions. The formation and growth of magnetite on Fe-EC electrodes has been documented by a number of field and laboratory Fe-EC studies (Müller et al. 2019; van Genuchten et al. 2016; Timmes et al. 2010). The predominance of magnetite in our work is attributed to the initial product of Fe-EC treatment being Fe(II) and the high thermodynamic stability of magnetite across a wide range of solution composition (i.e. pH, redox conditions) when Fe(II) is present (Cornell and Schwertmann 2003). The existence of magnetite in the surface layer interior is a concern because it has been proposed to trap electrochemically-generated Fe(II), which increases magnetite layer growth at the expense of Fe(II) transport to the bulk solution where As removal occurs. Magnetite formation is also important because its conductivity, though lower than bare Fe(0) metal, is orders of magnitude higher than that of most Fe(III) precipitates (e.g. lepidocrocite, goethite) and calcite, which is beneficial for the flow of current.

The greater abundance of calcite and Fe(III) precipitates in the exterior surface layers of the A-I and A-III regions is attributed to the design of the Fe-EC reactor. Though speculative, one explanation for preferential calcite formation near the electrode top is the proximity of this region to the air-water interface. This proximity could facilitate calcite formation by more effective $CO_{2(g)}$ exchange with the atmosphere (exsolving increases pH and favors calcite formation) or by mixing-induced splashes near the water surface enhancing evaporation and leading to locally increased Ca^{2+} and CO_3^{2-} activity. The color and abundance of Fe(III) precipitates in the A-III region of all 32 electrodes is likely related to the accumulation of settled

solids at the bottom of the reactor tanks. Due to the flat bottom of the reactor tanks and insufficient pumping of the post-electrolysis suspension to the tube settler, a constant layer of settled particles remained in the tanks after water transfer. This layer of accumulated sludge consisted of the poorly-ordered Fe(III) precipitates formed during typical Fe-EC treatment (Fig. S4) and was ~10 cm deep under stagnant conditions. However, when the tanks were filled and mixed, a fraction of this layer became resuspended, leading to a dense region of solids near the bottom of the reactor, consistent with the adherence of orange, poorly-ordered Fe(III) precipitates to the A-III region of the electrode (Fig. 2, Fig. S4). While the light-colored surface layers in the A-I and A-III regions can inhibit Fe(II) transport to the bulk solution similar to magnetite, these surface layers also likely lead to inhomogeneous electron flow through the electrodes. The insulating surface layer minerals (e.g. calcite, Fe(III) precipitates) in the A-I and A-III regions are expected to result in preferential electron flow through the A-II region. This conclusion is consistent with the significant quantities of uncorroded Fe(0) metal in the A-I and A-III regions observed after deep cleaning (Fig. 2B) and only a few spots of bare Fe(0) metal in the A-II region, suggesting nearly complete electrochemical oxidation of the center of the electrode.

4.1.2 Blisters. In addition to the three horizontal regions of distinct surface layers, another major modification of the electrode surface was the formation of protruding blisters (2-5 cm wide) of rusted Fe(0) metal. These blisters were most abundant and had the largest diameter in the A-II region (Fig. 2B), where the electrodes were likely most electrochemically active, but blistering was observed to a lesser extent in the A-I and A-III regions. These unique features can be explained by the cathodic reduction of H^+. The reaction occurring at the cathode most commonly reported in the Fe-EC literature is the reduction of $2H^+$ to form $H_{2(g)}$ that bubbles to the water surface. However, it is well documented that H^+ reduction can also yield adsorbed H atoms that diffuse into the Fe(0) crystal lattice to occupy microstructural defect sites, such as

vacancies, dislocations and grain boundaries (Landolt 2007; Jiang and Carter 2004; Bockris et al. 1965). At these sites, $H_{2(g)}$ build-up from H atom recombination can create local areas of high internal pressure, which causes deformation and pushes the material towards the surface, consistent with our observations of dome-shaped blisters (Laureys et al. 2017; Escobar et al. 2011). Since the electrode polarity of the investigated Fe-EC system was reversed between every test (i.e. each electrode served as cathode and anode), every electrode was blistered. The only regions without blisters were the sides of the four end-plates (E1, E16, E17, E32) facing the bulk electrolyte (Fig. S2), which is consistent with their lower current and interface potentials (Table S4, Fig. S5).

The formation of relatively large blisters is a concern for Fe-EC system operation because they worsen the structural integrity of the Fe(0) electrodes. Because Fe-EC is based on forming Fe(II) by the oxidation of the Fe(0) anode (often termed the *sacrificial* anode), it is inevitable that the electrodes must be replaced when all Fe(0) metal has been oxidized. However, the electrode must be replaced more quickly if uncorroded Fe(0) is still present, but the electrode fails structurally. In our work, deep cleaning of a blister on one electrode removed a large flake of magnetite, leaving a small hole in the plate. Removal of many similarly large flakes could therefore result in large holes and failure of the electrode structure, which would lead to the premature loss of beneficial, uncorroded Fe(0) metal. However, we note that so long as the structural integrity of the electrode is maintained, the formation of large blisters is expected to be less consequential to Fe-EC performance than the coating of the electrode surface by insulating layers of calcite and Fe(III) precipitates.

4.2 Influence of electrode deep cleaning on solution chemistry

4.2.1 Iron. The optimization of Fe-EC performance relies on efficient electrochemical Fe(II) production and transport to the bulk solution. We found that electrode deep cleaning

increased the bulk Fe concentration after electrolysis from <15 mg/L to 41.5 mg/L, a nearly 3-fold improvement, and decreased the total cell voltage by ~2V. We note that bulk Fe levels might have continued to increase following the electrolysis stage due to insufficient electrolyte mixing, but no measurements were collected after the current stopped. This clear improvement in Fe release to solution after electrode deep cleaning provides compelling field-based evidence to confirm the hypothesis that electrode surface layers block the transport of electrochemically generated Fe(II) to the bulk electrolyte. Because the production and release of Fe(II) from the electrode initiates the removal of many chemical species in Fe-EC, the increased bulk Fe level coincided with more effective removal of As, P, Si and Mn and modified the behavior of DO and solution pH. The chemical dynamics of As, DO and pH before and after cleaning are discussed below, with P, Si and Mn removal described in section S2 of the ESM.

4.2.2 Arsenic. Before deep cleaning, ~90 min of Fe(0) electrolysis was required to remove 164±9 µg/L As to below the 10 µg/L WHO MCL, which equated to >2.2 kWh (average voltage of 9.9 V). It is noteworthy that the uncleaned electrodes still achieved adequate As removal despite poor bulk Fe production, which could be partly due to the high raw water Fe content and the resuspension of reactive Fe(III) precipitates that had settled in the reactor tank bottoms during previous runs. After deep cleaning, only 60 min of electrolysis was required to achieve <10 µg/L As, which equated to 1.3 kWh (average voltage of 8.4 V). Therefore, if electrolysis ceased after 60 min when the As level decreased to <10 µg/L, the As removal efficiency would be nearly twice as high after electrode deep cleaning (increase from 72.9 to 128.4 µg/L As per kWh). However, additional electrolysis time included as a factor of safety resulted in only 20% higher As removal efficiency after electrode deep cleaning (increase from 72.9 to 86.4 µg/L/kWh). Previous laboratory studies of Fe-EC systems operated at similar charge dosage rates as the pilot plant indicate that arsenic removal typically proceeds through a two-step pathway (Li et al. 2012, van Genuchten et al. 2012, van Genuchten et al. 2020): i)

476 oxidation of arsenite (As(III)), the dominant species in reduced aquifers (Roberts et al. 2004), by
477 reactive Fenton-type oxidants (e.g. Fe(IV)) generated by Fe(II) reactions with DO and ii)
478 arsenate (As(V)) sorption to co-precipitating Fe(III) (oxyhydr)oxides. This reaction pathway is
479 supported by As K-edge XAS measurements of the arsenic-rich sludge collected directly from
480 the pilot plant, which indicated that As(V) is the overwhelmingly dominant form of arsenic
481 bound to the solids (Roy et al. 2019). Since both reaction steps are initiated by Fe(II), the
482 improvement in As removal efficiency can be explained by the increased bulk Fe concentration
483 and the lower total cell voltage (hence lower electrical energy consumption) after electrode deep
484 cleaning. We note briefly here that while the sludge contains strongly-sorbing As(V), appropriate
485 sludge disposal is still necessary because aqueous As can leach even from As(V)-rich Fe(III)
486 oxides when the solids are exposed to reducing conditions (e.g. organic-rich soils). In the short
487 term, the sludge generated at the plant is being used by researchers at Jadavpur University for
488 investigating its immobilization in concrete blocks (Roy et al. 2019). For the long term, a
489 contract has been signed with a state-approved hazardous waste disposal company (Ramky Ltd.)
490 for removing sludge for storage at a hazardous chemical waste disposal site at Haldia, West
491 Bengal (Hernandez et al. 2019).

492 Another outcome of removing and characterizing the electrode surface layers is the
493 ability to perform a mass balance calculation of As on a large Fe-EC system to confirm the As
494 removal location. Averaging the composition of surface layer samples measured in this work
495 (Table S2) gives a surface layer As content of 51.7±39.5 mg/kg. Multiplying this value by the
496 surface layer mass removed during deep cleaning gives a total of 3.82±2.92 g of As attached to
497 the electrode. During the two years of surface layer growth, the plant treated ~900 m^3 of
498 groundwater from 164±9 to <10 µg/L As (i.e. at least 154 µg/L removed), yielding 138.6 g of
499 total As removed. These calculations indicate that As attachment to the electrode surface
500 accounted for <3% of total removal, which supports the conclusion that As is removed

dominantly by sorption to Fe(III) precipitates in the bulk (Kumar et al. 2004). We note that the As content of the light-colored layers was several times higher than for magnetite, suggesting that the As fraction bound to the electrodes would decrease further if Fe(III) precipitate build-up on the electrode was avoided.

4.2.2 Dissolved oxygen and solution pH. In addition to altering the dynamics of ion removal, electrode deep cleaning also affected the behavior of DO and solution pH. Measurements of DO during experiments with both unclean and clean electrodes revealed a continuous increase from the low initial value (<2.0 mg/L) throughout electrolysis, which indicates that the flux of atmospheric O_2 into the electrolyte was greater than O_2 consumption during Fe-EC treatment. However, the final DO was ~2 mg/L lower after deep cleaning than before, which can be explained by the more efficient production of Fe(II) with clean electrodes, which consumes DO to form Fe(III) precipitates (Delaire et al. 2017). In experiments with both unclean and clean electrodes, the solution pH increased steadily during electrolysis, which is explained by a combination of both $CO_{2(g)}$ outgassing and the consumption of H^+ ions at the cathode. However, after deep cleaning, the pH increase was 0.15-0.2 log units lower than before deep cleaning. This result is attributed to the higher bulk Fe concentration after deep cleaning because Fe(II) oxidation and Fe(III) hydrolysis consumes OH^-, thus lowering pH.

4.3 Recommendations for maintaining and operating Fe-EC systems

Proper maintenance of water treatment technologies is critical to ensure their sustained operation in optimal conditions. This is particularly important when operating in rural, resource-poor areas where small changes in overall treatment costs and power consumption can render technologies ineffective or economically unviable. In our study, we investigated one of the only documented Fe-EC pilot plants that has sustainably removed arsenic from local groundwater in South Asia for extended periods (about 4 years at the time of this writing). Studying this unique

system, we found that mechanically removing the magnetite, calcite and Fe(III) precipitate surface layers formed on Fe(0) electrodes over extended operation improved dramatically the performance of the system. For example, surface layer removal resulted in a substantial increase in bulk Fe production and a decrease in the voltage (and hence in the electrical energy consumption) required to pass the 150 A of current needed for treatment. These improvements led to a significant increase in arsenic removal efficiency (128.4 μg/L As removed per kWh after cleaning, 72.9 μg/L As removed per kWh before cleaning). These results imply that periodic, on-schedule electrode cleaning to completely remove accumulated surface layers can help to sustain the performance of Fe-EC systems over year-long timescales. Based on cost estimates of local labor and electricity use, our cost-benefit analysis (Table S5) suggests that the cleaning procedure was economically practical, but we note that the success criteria for maintaining different Fe-EC plants will depend on regional costs of labor and electricity and several properties of the plant (e.g. size, influent arsenic concentration, price of steel, etc).

Among the various approaches to maintain Fe-EC electrodes reported in the literature (e.g. ultrasonic cleaning, high electrolyte velocity gradients: see section S3 in the ESM), mechanical abrasion is one of the most attractive for rural communities in South Asia because this method is simple, reliable and low-cost (Amrose et al. 2014, Hernandez et al. 2019, Timmes et al. 2010, van Genuchten et al. 2016). Although this method requires some labor and equipment, only three minimally trained workers were able to perform the deep cleaning in less than two days, indicating the relative ease of the task. This suggests that the entire procedure could be completed in a single weekend, which would prevent disrupting water treatment and distribution to students, teachers, and staff during hours when the school that houses the pilot plant is open. While polarity reversal has been proposed as a method to minimize surface layer growth, our results suggest that this strategy had minimal effect, which is consistent with a laboratory Fe-EC study showing polarity reversal actually increased surface layer growth over

extended operation (Muller et al. 2019). One promising alternative could be to operate the system at high current densities (i.e. i >3 mA/cm^2), which was recently shown at the lab-scale to limit surface layer formation (Muller et al. 2019), but this approach has not been tested on large Fe-EC systems and can result in unacceptably high voltages. Hence, we propose that mechanical deep cleaning is one of the most promising methods to improve bulk Fe(II) production and decrease energy requirements, which is essential to achieve consistent As removal over sustained periods.

The precise timing of electrode cleaning will depend on the operating conditions and reactor design of the specific Fe-EC system, but our study has uncovered some useful relationships to help optimize and simplify the cleaning schedule. One of the most obvious indicators of Fe-EC performance and a useful trigger for electrode maintenance is the bulk Fe concentration, which could be monitored regularly using field test kits (Merrill et al. 2009) However, routine Fe measurements require trained labor and can be prohibitively expensive, particularly in poor, decentralized communities. Instead, a number of other indicators could be used, including the DO, solution pH and total cell potential. In our work, we found that behaviors of the DO, pH and the cell voltage were all impacted by deep cleaning, with systematic changes concomitant with an increase in bulk Fe concentration. These parameters are simple to measure using hand-held devices, with unambiguous numerical values (as opposed to color-based test kits). Therefore, plant operators without formal education can easily track the behavior of the DO, pH and cell voltage and compare the values produced using clean electrodes with those of old electrodes to make more informed decisions of when to begin an electrode deep cleaning activity.

Finally, with respect to electrode blistering, we found that intensive mechanical cleaning around blisters could lead to holes through the electrode, which should be avoided to maintain the structural integrity of the electrode. Therefore, we recommend that electrode deep cleaning

preferentially targets the light-colored external electrode surface layers, which are significantly more insulating than the magnetite interior layers and are the region most likely to overlay bare Fe(0) metal. In addition, different types of steel of can be used as the electrode material since the steel production process can impact the likelihood of blister formation. For example, a recent study showed that cold formed steel allows the growth of blisters more than recovered and recrystallized steel because of a greater number of structural defects (Laureys et al. 2017). The electrode material used in the investigated Fe-EC system was cold formed steel, which could contribute to the large sized blisters. Since H^+ reduction is likely related to blister formation, selecting electrode materials that favor other cathodic reactions, such as carbon-based air-diffusion cathodes that reduce O_2 form OH^- or H_2O_2 (Jiang et al. 2018) could also prevent the electrode blistering observed in this work.

This paper appears in Water Research (2020). DOI:10.1016/j.watres.2020.115668

5. Conclusions

- Thick surface layers formed on Fe-EC electrodes following operation over two years, which inhibited Fe(II) transport to the bulk electrolyte. Surface layer growth occurred despite polarity reversal between tests.
- Three distinct horizontal surface layer regions formed: Fe(III) precipitates, calcite and magnetite at the top, magnetite in the middle and Fe(III) precipitates and magnetite at the bottom. The surface layer stratification is attributed to the operating conditions and Fe-EC reactor design.
- The middle region of all electrodes, which was dominated by magnetite and likely the most electrochemically active area, consisted of 2-5 cm blisters attributed to cathodic H^+ reduction and H diffusion into the Fe(0) metal.
- Mechanical removal of the surface layers increased substantially the bulk Fe concentration, decreased total cell voltage and improved the removal efficiency of As and other ions.
- Our work suggests that periodic, on-schedule electrode cleaning by mechanical abrasion can sustain Fe-EC performance over year-long timescales.

6. Acknowledgements

We acknowledge funding provided by the Dutch Organization for Scientific Research in a Veni Grant to CMvG (Project No. 14400). SRSB gratefully acknowledges support from Andrew and Virginia Rudd Family Foundation Chair Funds of Prof. Gadgil, and from a CHED funded project at UC Berkeley on ECAR research for application in the Philippines. We gratefully acknowledge guidance from Joyashree Roy and Anupam DebSarkar (Jadavpur University) and technical assistance from Sebastian Krogh during the field experiments. Synchrotron experiments were performed partly at the DUBBLE beam line at the ESRF, Grenoble, France, with assistance from Dipanjan Banerjee. We also thank Ryan Davis for technical support during synchrotron data collection at SSRL. Use of SSRL, SLAC National Accelerator Laboratory, was supported by the U.S. Department of Energy, Office of Science, Basic Energy Sciences, under Contract No. DE-AC02-76SF00515.

Figure Captions

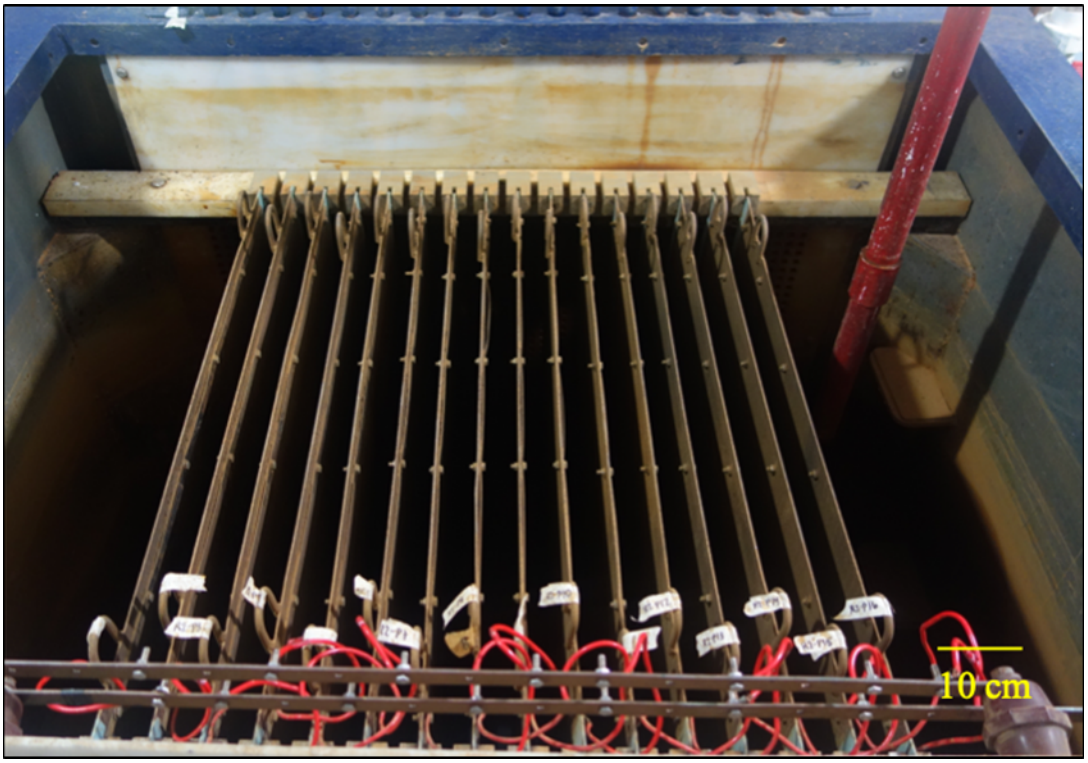

Fig. 1: Top view of the electrode assembly in reactor tank 1. Electrodes shown in this picture are numbered E1 to E16 (left to right). This electrode layout was reproduced in reactor tank 2, which housed electrodes E17 to E32.

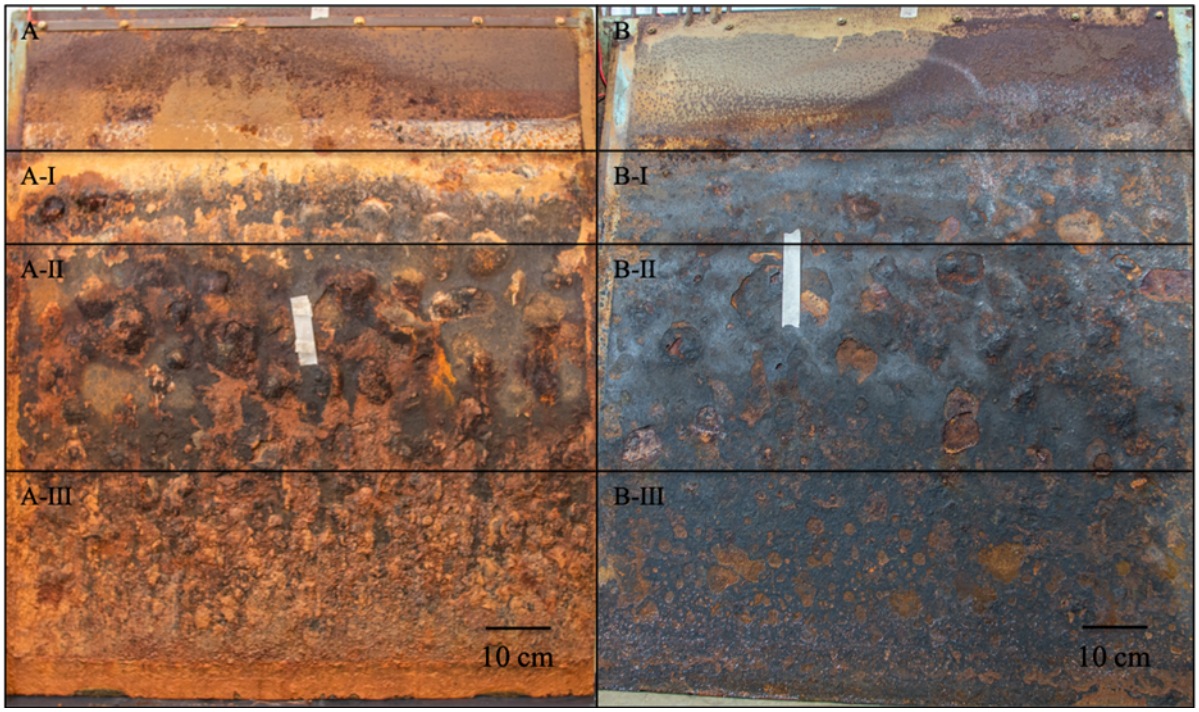

Fig. 2: A) Digital images representative electrodes before (A) and after (B) deep cleaning. All electrodes before deep cleaning displayed the A-I (top), A-II (middle) and A-III (bottom) regions. The regions above A-I and B-I were not in contact with the electrolyte solution during electrolysis and showed relatively little rust accumulation. The tape stuck to the electrode surface was added to help scale the dome-shaped blisters.

This paper appears in Water Research (2020). DOI:10.1016/j.watres.2020.115668

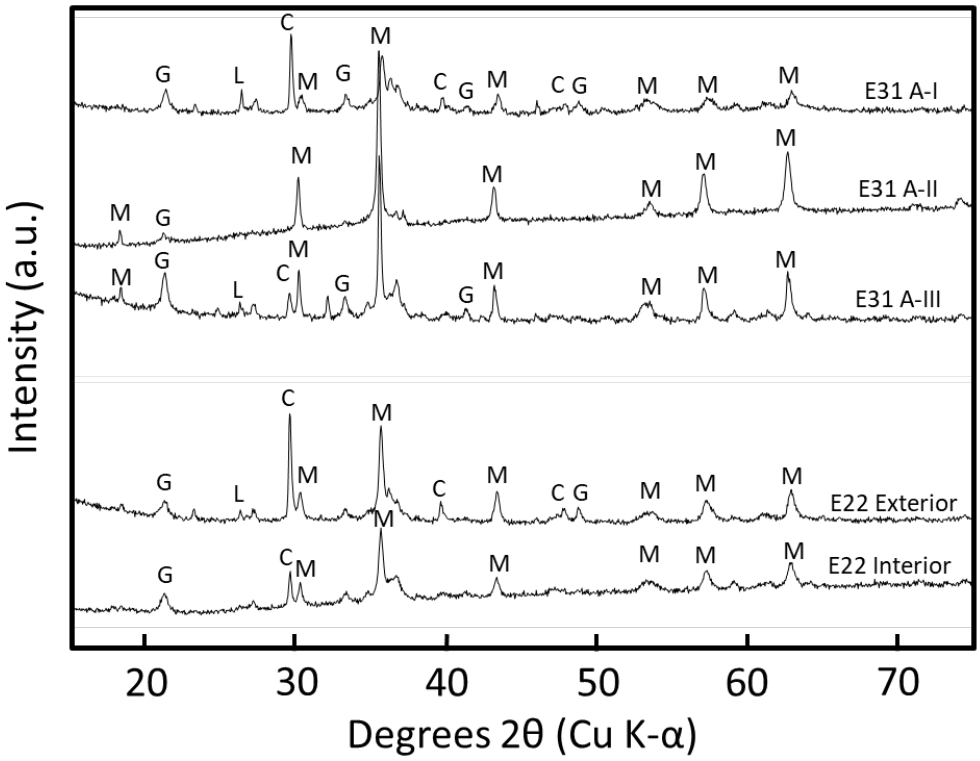

Fig. 3: Powder XRD patterns of surface layers collected from different regions of electrode E31 (A-I, A-II, A-III) and electrode E22 (Exterior, Interior). The letters M, G, L and C represent the diffraction peaks of magnetite, goethite, lepidocrocite and calcite, respectively.

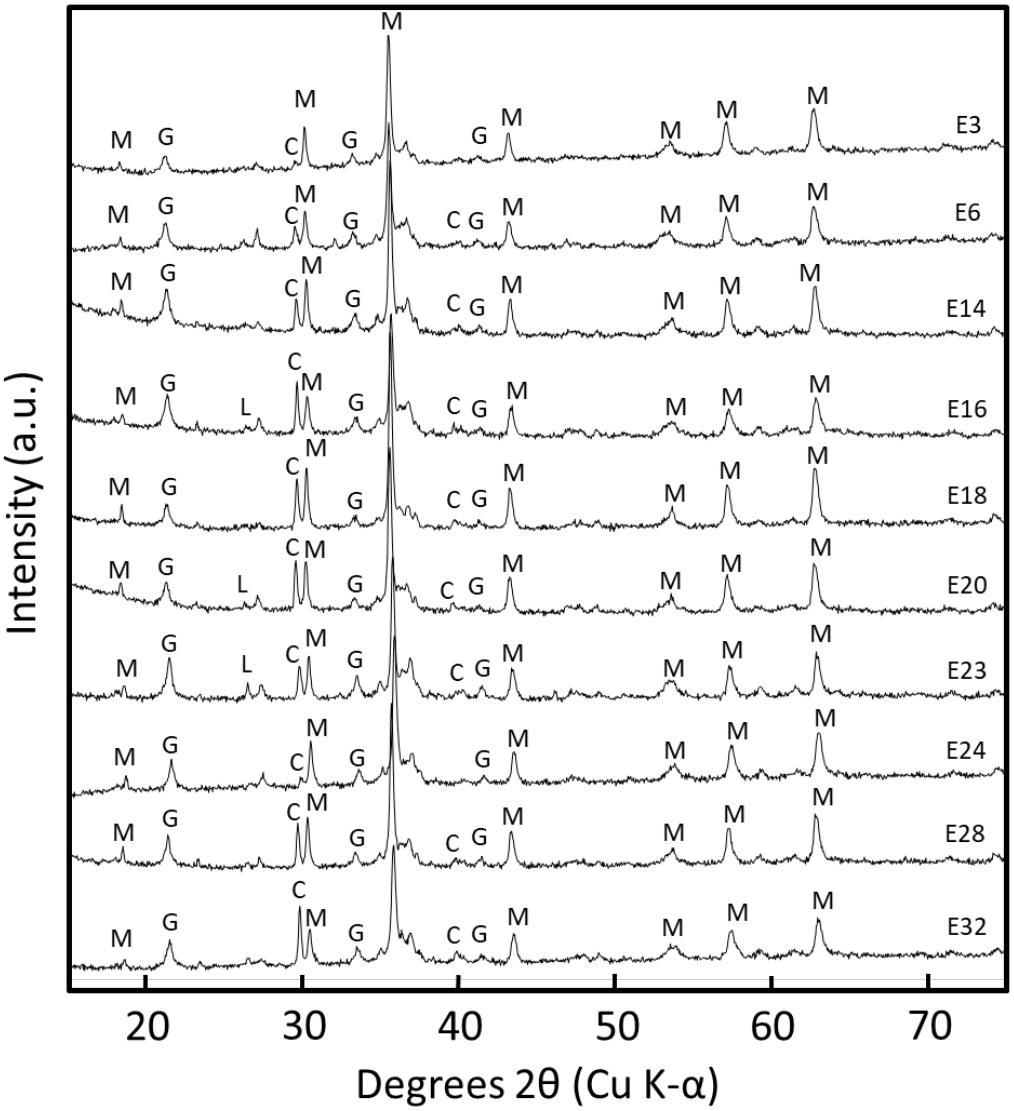

643
644
645 Fig. 4: Powder XRD patterns of surface layers collected from select electrodes. The letters M, G,
646 L and C represent the diffraction peaks of magnetite, goethite, lepidocrocite and calcite,
647 respectively.
648
649

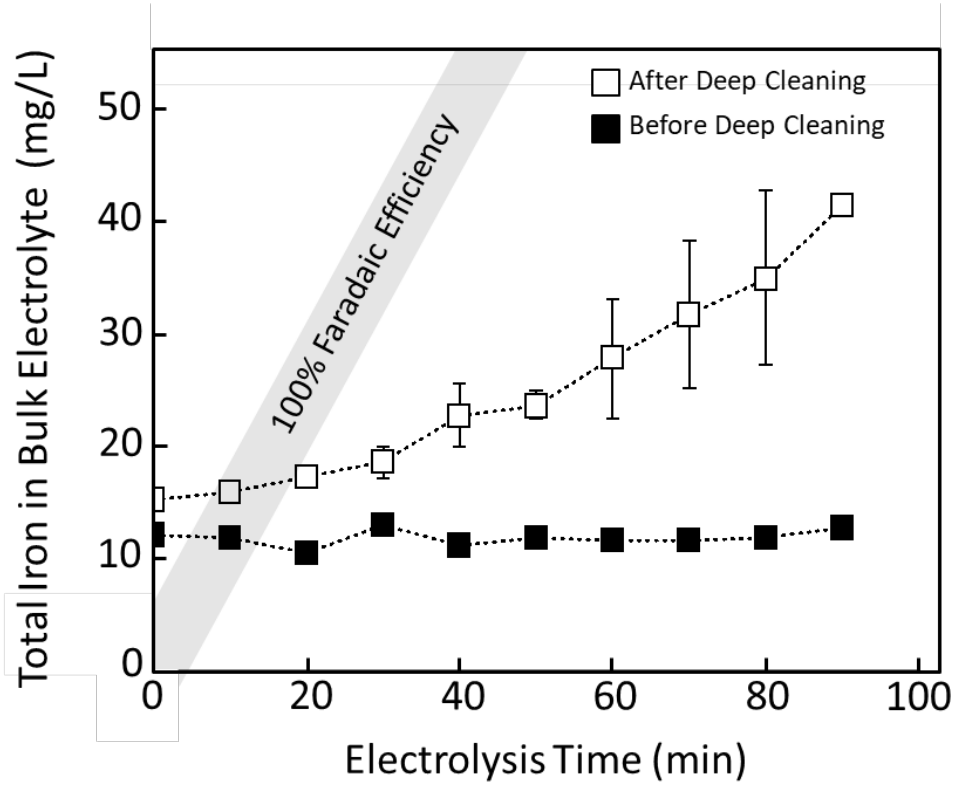

650
651
652 Fig. 5: Total (aqueous plus solid phase) iron concentration in the bulk electrolyte as a function
653 of electrolysis time, for experiments before (black squares) and after electrode deep cleaning
654 (white squares). 450 C/L was delivered by Fe(0) electrolysis over approximately 90 minutes.
655 The gray shaded region indicates the value expected based on 100% Faradaic efficiency.
656
657

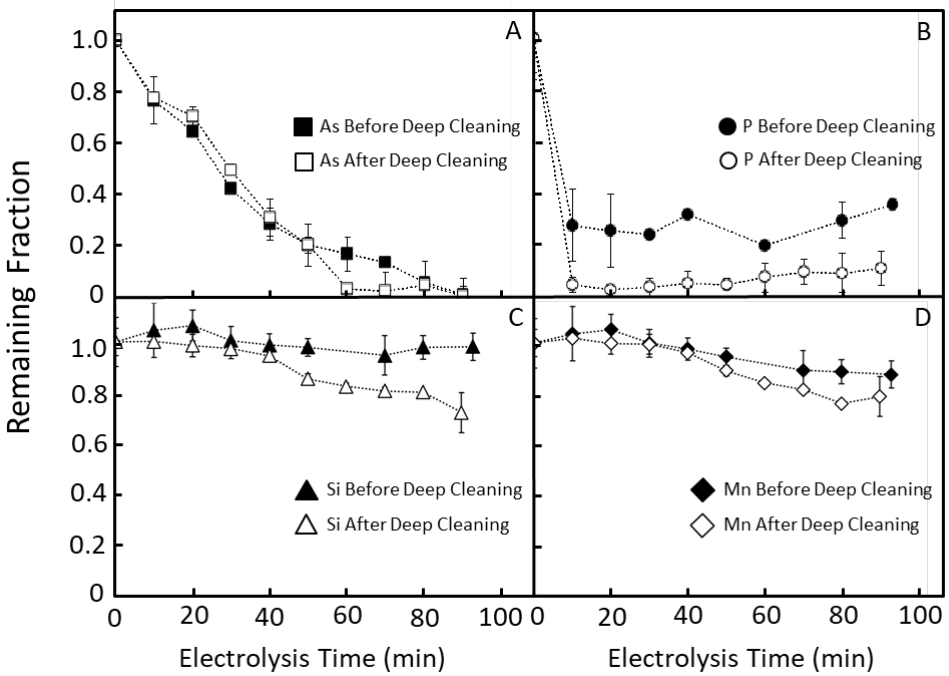

Fig. 6: Fraction of initial aqueous arsenic (A), phosphate (B), silicate (C) and manganese (D) remaining in the bulk solution as a function of electrolysis time. The black diamonds indicate measurements before deep cleaning, whereas the white diamonds indicate measurements after deep cleaning.

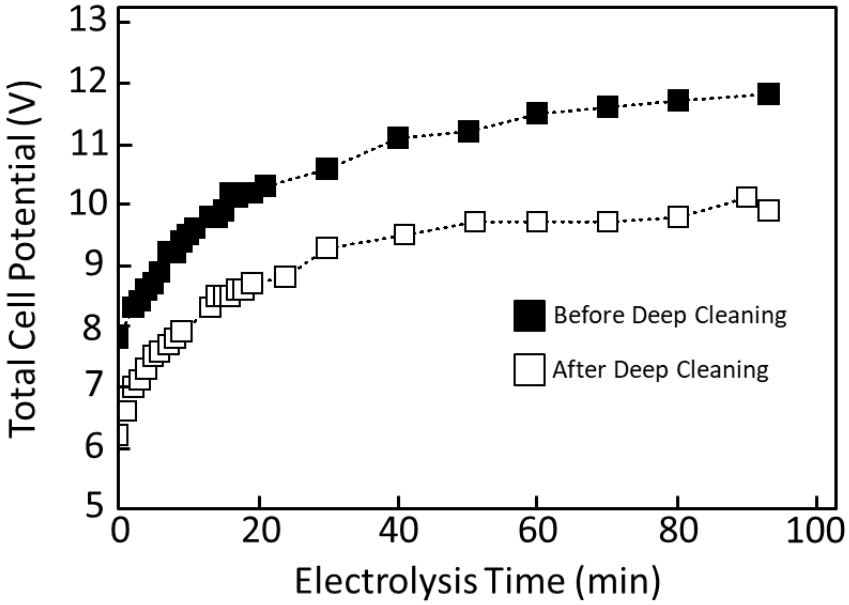

Fig. 7: Total cell potential as a function of electrolysis time for experiments before (black squares) and after (white squares) electrode deep cleaning.

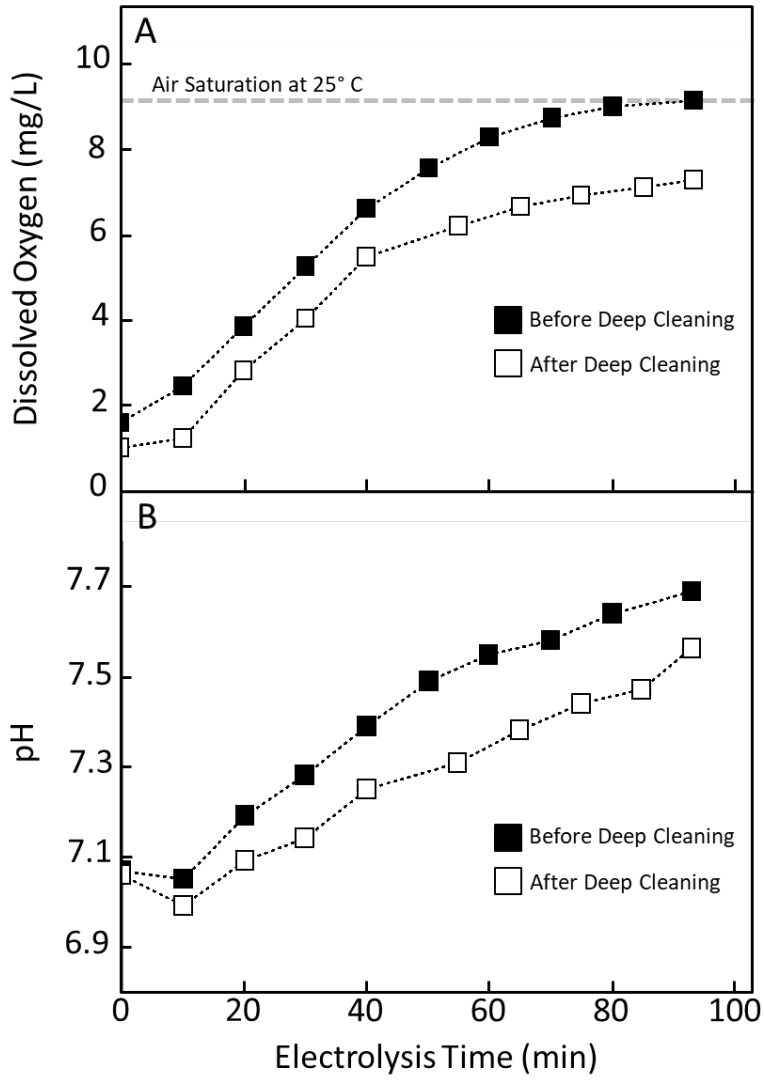

672
673
674 Fig. 8: Dissolved oxygen (top panel) and solution pH (bottom panel) as a function of electrolysis
675 time for experiments before (black squares) and after (white squares) electrode deep cleaning.
676 Data points represent measurements in reactor tank 1.
677
678

This paper appears in Water Research (2020). DOI:10.1016/j.watres.2020.115668

679 **Table 1: Chemical composition of air-dried sludge and select electrode surface layers**

Sample Name	Chemical Composition										
	Fe (g/kg)	As (mg/kg)	As/Fe (mol%)	P (mg/kg)	P/Fe (mol%)	Si (mg/kg)	Si/Fe (mol%)	Ca (g/kg)	Ca/Fe (mol%)	Mn (mg/kg)	Mn/Fe (mol%)
Air Dried Sludge	186	864.0	0.346	5320	5.16	6684	7.16	71.3	53.5	885	0.48
E31Region A-I	450	158.2	0.026	497	0.20	5507	2.43	42.9	13.3	1057	0.24
E31Region A-II	532	55.0	0.008	658	0.22	3072	1.15	1.9	0.50	1006	0.19
E31 Region A-III	435	71.9	0.012	654	0.27	5388	2.46	24.6	7.89	770	0.18
E22 Exterior	456	245.0	0.040	761	0.30	5268	2.30	69.9	21.4	1174	0.26
E22 Interior	460	ND	ND	348	0.14	1281	0.55	15.8	4.78	880	0.19

680 Values were obtained from aqua regia digestions. The remaining mass fraction is attributed to oxygen.
681

References

Amrose, S., Z. Burt, and I. Ray. 2015. Safe Drinking Water for Low-Income Regions, *Annual Review of Environment and Resources, Vol 40*, 40: 203-31.

Amrose, S. E., S. R. S. Bandaru, C. Delaire, C. M. van Genuchten, A. Dutta, A. DebSarkar, C. Orr, J. Roy, A. Das, and A. J. Gadgil. 2014. Electro-chemical arsenic remediation: Field trials in West Bengal, *Science of the Total Environment*, 488: 543-50.

Amrose, S., A. Gadgil, V. Srinivasan, K. Kowolik, M. Muller, J. Huang, and R. Kostecki. 2013. Arsenic removal from groundwater using iron electrocoagulation: Effect of charge dosage rate, *Journal of Environmental Science and Health Part a-Toxic/Hazardous Substances & Environmental Engineering*, 48: 1019-30.

Borsboom, M, W Bras, I Cerjak, D Detollenaere, DG van Loon, P Goedtkindt, M Konijnenburg, P Lassing, YK Levine, B Munneke, M Oversluizen, R van Tol, and E Vlieg. 1998. The Dutch-Belgian beamline at the ESRF, *Journal of Synchrotron Radiation*, 5: 518-20.

Chen, G. H. 2004. Electrochemical technologies in wastewater treatment, *Separation and Purification Technology*, 38: 11-41.

Cornell, R. M. and Schwertmann, U. 2003. *The iron oxides: structure, properties, reactions, occurrences and uses*. John Wiley & Sons. Marcus, P. ed., 2011. Corrosion mechanisms in theory and practice. CRC press.

Delaire, C., S. Amrose, M. H. Zhang, J. Hake, and A. Gadgil. 2017. How do operating conditions affect As(III) removal by iron electrocoagulation ?, *Water Research*, 112: 185-94.

Escobar, D. P., C. Minambres, L. Duprez, K. Verbeken, and M. Verhaege. 2011. Internal and surface damage of multiphase steels and pure iron after electrochemical hydrogen charging, *Corrosion Science*, 53: 3166-76.

Hernandez, D., K. Boden, P. Paul, S.R.S. Bandaru, S. Mypati, A. Roy, S.E. Amrose, J. Roy, A.J. Gadgil. 2019. Strategies for successful field deployment in a resource-poor region: Arsenic remediation technology for drinking water, *Development Engineering*, 4.

Holt, P. K., G. W. Barton, and C. A. Mitchell. 2005. The future for electrocoagulation as a localised water treatment technology, *Chemosphere*, 59: 355-67.

Hug, S. J., and O. Leupin. 2003. Iron-catalyzed oxidation of arsenic(III) by oxygen and by hydrogen peroxide: pH-dependent formation of oxidants in the Fenton reaction, *Environmental Science & Technology*, 37: 2734-42.

Jiang, D.E. and Carter, E.A. 2004. Diffusion of interstitial hydrogen into and through bcc Fe from first principles. *Physical Review B*,*70*(6), p.064102.

Jiang, Y. Y., P. J. Ni, C. X. Chen, Y. Z. Lu, P. Yang, B. Kong, A. Fisher, and X. Wang. 2018. Selective Electrochemical H2O2 Production through Two-Electron Oxygen Electrochemistry, *Advanced Energy Materials*, 8.

Johnston, R. B., S. Hanchett, and M. H. Khan. 2010. The socio-economics of arsenic removal, *Nature Geoscience*, 3: 2-3.

Kumar, P. R., S. Chaudhari, K. C. Khilar, and S. P. Mahajan. 2004. Removal of arsenic from water by electrocoagulation', *Chemosphere*, 55: 1245-52.

Lakshmanan, D., D. A. Clifford, and G. Samanta. 2009. Ferrous and Ferric Ion Generation During Iron Electrocoagulation, *Environmental Science & Technology*, 43: 3853-59.

Landolt, Dieter. 2007. *Corrosion and surface chemistry of metals* (EPFL Press ; CRC Press distributor: Lausanne Boca Raton, FL).

Laureys, A., E. Van den Eeckhout, R. Petrov, and K. Verbeken. 2017. Effect of deformation and charging conditions on crack and blister formation during electrochemical hydrogen charging, *Acta Materialia*, 127: 192-202.

731 Merrill, R. D., A. A. Shamim, A. B. Labrique, H. Ali, K. Schulze, M. Rashid, P. Christian, and
732 K. P. West. 2009. Validation of two Portable Instruments to Measure Iron concentration
733 in Groundwater in rural Bangladesh, *Journal of Health Population and Nutrition*, 27:
734 414-18.
735 Moreno, H. A., D. L. Cocke, J. A. G. Gomes, P. Morkovsky, J. R. Parga, E. Peterson, and C.
736 Garcia. 2009. Electrochemical Reactions for Electrocoagulation Using Iron Electrodes,
737 *Industrial & Engineering Chemistry Research*, 48: 2275-82.
738 Müller, S., T. Behrends, and C. M. van Genuchten. 2019. Sustaining efficient production of
739 aqueous iron during repeated operation of Fe(0) electrocoagulation, Water Research, 155:
740 455-464.
741 Naujokas, M. F., B. Anderson, H. Ahsan, H. V. Aposhian, J. H. Graziano, C. Thompson, and W.
742 A. Suk. 2013. The Broad Scope of Health Effects from Chronic Arsenic Exposure:
743 Update on a Worldwide Public Health Problem, *Environmental Health Perspectives*, 121:
744 295-302.
745 Nikitenko, S, AM Beale, AMJ van der Eerden, SDM Jacques, O Leynaud, MG O'Brien, D
746 Detollenaere, R Kaptein, BM Weckhuysen, and W Bras. 2008. Implementation of a
747 combined SAXS/WAXS/QEXAFS set-up for time-resolved in situ experiments, *Journal*
748 *of Synchrotron Radiation*, 15: 632-40.
749 Nikolaev, NV, AS Kozlovskii, and II Utkin. 1982. Treating natural waters in small water
750 systems by filtration with electrocoagulation, *Soviet Journal of Water Chemistry and*
751 *Technology*, 4: 244-47.
752 Roberts, L. C., S. J. Hug, T. Ruettimann, M. Billah, A. W. Khan, and M. T. Rahman. 2004.
753 Arsenic removal with iron(II) and iron(III) in waters with high silicate and phosphate
754 concentrations, *Environmental Science & Technology*, 38: 307-15.
755 Roy, A., van Genuchten, C.M., Mookherjee, I., Debsarkar, A. and Dutta, A. 2019. Concrete
756 stabilization of arsenic-bearing iron sludge generated from an electrochemical arsenic
757 remediation plant. *Journal of environmental management*, *233*, pp.141-150.
758 Smith, A. H., C. Hopenhayn-Rich, M. N. Bates, H. M. Goeden, I. Hertz-Picciotto, H. M.
759 Duggan, R. Wood, M. J. Kosnett, and M. T. Smith. 1992. Cancer risks from arsenic in
760 drinking water, *Environ Health Perspect*, 97: 259-67.
761 Smith, A. H., P. A. Lopipero, M. N. Bates, and C. M. Steinmaus. 2002. Public health - Arsenic
762 epidemiology and drinking water standards, *Science*, 296: 2145-46.
763 Steinmaus, C. M., C. Ferreccio, J. A. Romo, Y. Yuan, S. Cortes, G. Marshall, L. E. Moore, J. R.
764 Balmes, J. Liaw, T. Golden, and A. H. Smith. 2013. Drinking water arsenic in northern
765 chile: high cancer risks 40 years after exposure cessation, *Cancer Epidemiol Biomarkers*
766 *Prev*, 22: 623-30.
767 Tiegel, M. C., M. L. Martin, A. K. Lehmberg, M. Deutges, C. Borchers, and R. Kirchheim. 2016.
768 Crack and blister initiation and growth in purified iron due to hydrogen loading, *Acta*
769 *Materialia*, 115: 24-34.
770 Timmes, T. C., H. C. Kim, and B. A. Dempsey. 2010. Electrocoagulation pretreatment of
771 seawater prior to ultrafiltration: Pilot-scale applications for military water purification
772 systems, *Desalination*, 250: 6-13.
773 van Genuchten, C.M., Addy, S.E., Peña, J. and Gadgil, A.J. 2012. Removing arsenic from
774 synthetic groundwater with iron electrocoagulation: an Fe and As K-edge EXAFS study.
775 *Environmental science & technology*, *46*(2), pp.986-994.
776 van Genuchten, C. M., S. R. S. Bandaru, E. Surorova, S. E. Amrose, A. J. Gadgil, and J. Pena.
777 2016. Formation of macroscopic surface layers on Fe(0) electrocoagulation electrodes
778 during an extended field trial of arsenic treatment, *Chemosphere*, 153: 270-79.

van Genuchten, C. M., K. N. Dalby, M. Ceccato, S. L. S. Stipp, and K. Dideriksen. 2017. Factors affecting the Faradaic efficiency of Fe(0) electrocoagulation, *Journal of Environmental Chemical Engineering*, 5: 4958-68.

van Genuchten, C. M., and J. Pena. 2017. Mn(II) Oxidation in Fenton and Fenton Type Systems: Identification of Reaction Efficiency and Reaction Products, *Environmental Science & Technology*, 51: 2982-91.

van Genuchten, C. M., T. Behrends, S. L. S. Stipp, and K. Dideriksen. 2020. Achieving arsenic concentrations of <1 ug/L, by Fe(0) electrolysis: The exceptional performance of magnetite. *Water Research*, 168: 115170.

Wan, W., T. J. Pepping, T. Banerji, S. Chaudhari, and D. E. Giammar. 2011. Effects of water chemistry on arsenic removal from drinking water by electrocoagulation, *Water Research*, 45: 384-92.

WHO. 2018. Developing drinking-water quality regulations and standards: general guidance with a special focus on countries with limited resources. In. Geneva: World Health Organization. Licence: CC BY-NC-SA 3.0 IGO.